https://doi.org/10.5194/amt-2022-196
Preprint. Discussion started: 23 August 2022

Atmospheric Measurement Techniques Discussions

Estimation of raindrop size distribution and rain rate with infrared surveillance camera in dark conditions

Jinwook Lee[1], Jongyun Byun[1], Jongjin Baik[1], Changhyun Jun[1], Hyeon-Joon Kim[1]

[1]Department of Civil and Environmental Engineering, College of Engineering, Chung-Ang University example, Seoul, 06974, South Korea

Correspondence to: Hyeon-Joon Kim (hjkim22@cau.ac.kr)

Abstract. This study estimated raindrop size distribution (DSD) and rainfall intensity with an infrared surveillance camera in dark conditions. Accordingly, rain streaks were extracted using a *k*-nearest neighbor (KNN)-based algorithm. The rainfall intensity was estimated using DSD based on physical optics analysis. The estimated DSD was verified using a disdrometer. Furthermore, a tipping-bucket rain gauge was used for comparison. The results are summarized as follows. First, a KNN-based algorithm can accurately recognize rain streaks from complex backgrounds captured by the camera. Second, the number concentration of raindrops obtained through closed-circuit television (CCTV) images was similar to the actual PArticle SIze and VELocity (PARSIVEL)-observed number concentration in the 0.5 to 1.5 mm section. Third, maximum raindrop diameter and the number concentration of 1 mm or less produced similar results during the period with a high ratio of diameters of 3 mm or less. Finally, after comparing with the 15-min cumulative PARSIVEL rain rate, the mean absolute percent error (MAPE) was 44%. The differences according to rain rate can be determined. The MAPE was 32% at a rain rate of less than 2 mm h^{-1} and 73% at a rate above 2 mm h^{-1}. We confirmed the possibility of estimating an image-based DSD and rain rate obtained based on low-cost equipment during dark conditions.

1 Introduction

Precipitation data is vital in water resource management, hydrological research, and global change analysis. The primary means of measuring precipitation is to use a rain gauge (Allamano et al., 2015) to collect raindrops from the ground. Due to the restrictions on the installation environment of the rain gauge, it is difficult to understand the spatial rainfall distribution in mountains and urban areas (Kidd et al., 2017). Furthermore, the tipping-bucket-type rain gauge, which accounts for most rain gauges, has a discrete observation resolution (0.1 or 0.5 mm) for the discrete time-steps, producing uncertainty in temporal rainfall variation.

In contrast, it is possible to obtain spatial rainfall information on a global scale with remote sensing techniques (Famiglietti et al., 2015). However, remote sensing techniques provide only indirect measurements that must be continuously calibrated and verified through ground-level precipitation measurements (Michaelides et al., 2009). Recently, a disdrometer capable of investigating the microphysics characteristics of rainfall has been used for observation instead of the traditional

https://doi.org/10.5194/amt-2022-196
Preprint. Discussion started: 23 August 2022

Atmospheric Measurement Techniques Discussions

rainfall observation instrument (Kathiravelu et al., 2016). However, these devices cannot be widely installed because of their high cost and difficulty in accessing observational data. Consequently, a high-resolution and low-cost ground precipitation monitoring network has not yet been established.

With the advent of the Internet of Things (IoT) era, using non-traditional sources is attractive for improving the spatio-temporal scale of existing observation networks (McCabe et al., 2017). In recent years, such cases have been common in rainfall observation. For example, there have been attempts to estimate rainfall using sensors to capture signal attenuation characteristics in commercial cellular communication networks (Overeem et al., 2016), vehicle wipers (Raibei et al., 2013), and smartphones (Guo et al., 2019). Furthermore, crowdsourcing information has been used to confirm the utility of estimating regional rainfall (Haberlandt and Sester, 2010; Rabiei et al., 2016; Yang and Ng, 2017).

In a similar context, a surveillance camera is a sensor with high potential. Surveillance cameras are often referred to as closed-circuit television (CCTV). Compared with other crowdsourcing methods, the visualization data of surveillance cameras are highly intuitive (Guo et al., 2017). Therefore, they have been used in various fields (Cai et al., 2017; Nottle et al., 2017; Hua, 2018). In Korea, public surveillance camera installations have been rapidly increasing, from approximately 150,000 in 2008 to 1.34 million in 2020—approximately a public CCTV camera per 0.07 km^2. Thus, the potential for precipitation estimation using camera sensing is expected to be greater in Korea.

Recently, various studies have been conducted to estimate rainfall intensity using the rain streak image obtained from surveillance camera videos. Many studies attempted to use artificial intelligence to capture changes in the image captured by the camera when it rains (Zen et al., 2019; Avanzato and Beritelli, 2020; Wang et al., 2022). In contrast, some studies have tried to estimate rainfall intensity using geometrical optics and photographic analyses. Typically, the rain streak layer is separated from the raw image or video. A rain streak is the visual appearance of raindrops caused by visual persistence—raindrops falling because of the blur phenomenon of raindrop movement from the camera's exposure time appears as streaks on the image. Garg and Nayar (2005) made one of the first attempts to measure this rainfall.

Since then, many studies have been conducted to develop and improve efficient algorithms. Allamano et al. (2015) proposed a framework to estimate the quantitative rainfall intensity using camera images based on physical optics from a hydrological perspective. Dong et al. (2017) proposed a more robust approach to identifying raindrops and estimating rainfall using a grayscale function, making grayscale subtraction nonlinear. Jiang et al. (2019) proposed an algorithm that decomposes rain-containing images into rain streak layers and rainless background layers using convex optimization algorithms and estimates instantaneous rainfall intensity through geometric optical analysis.

Some studies (e.g., Dong et al., 2017) have sought to estimate raindrop size distribution (DSD) using a surveillance camera. However, no study has estimated the rain in dark conditions to our knowledge. Furthermore, previous studies did not verify the estimated DSD using a disdrometer. In contrast, this study estimated DSD with an infrared surveillance camera in dark conditions, based on which rainfall intensity was also estimated. Rain streaks were extracted using a k-nearest neighbor (KNN)-based algorithm. The DSD was used to calculate rainfall intensity with physical optics analysis and verified using a PArticle SIze and VELocity (PARSIVEL) disdrometer.

https://doi.org/10.5194/amt-2022-196
Preprint. Discussion started: 23 August 2022

2 Methodology

Image-based rainfall estimation can be divided into two processes: identifying rainfall streaks and estimating DSD. Fig. 1 illustrates these processes in a flowchart. Identifying rain streaks requires an algorithm that separates the moving rain streaks from the background layer, as explained in Section 2.1. Next, in estimating DSD, raindrops are extracted from the image of the rain streaks, and the overall distribution is obtained. This process is explained in Section 2.2.

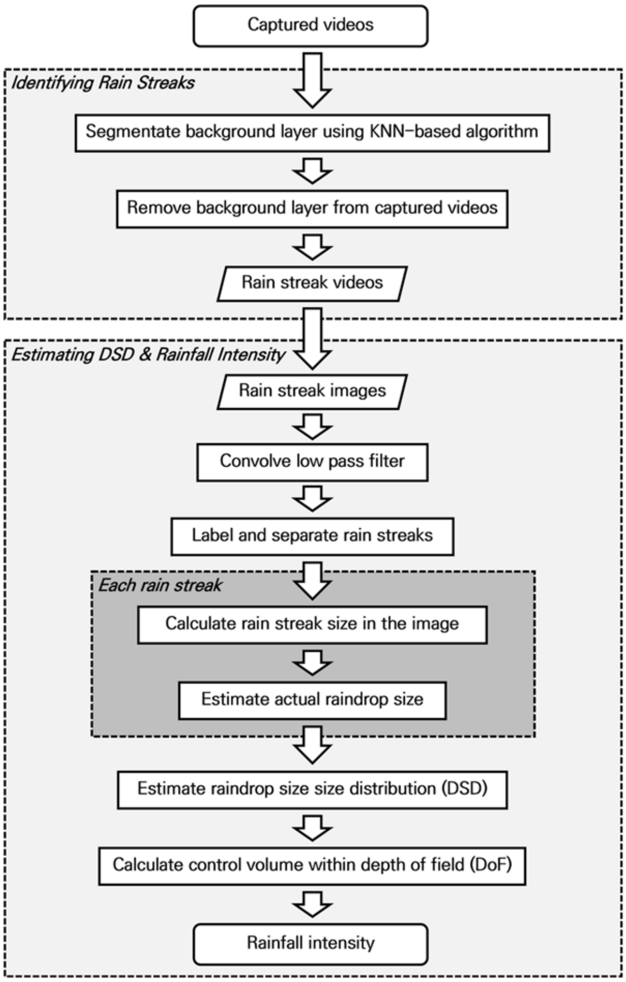

Figure 1: Flowchart of the methodology for estimating DSD and rainfall intensity

https://doi.org/10.5194/amt-2022-196
Preprint. Discussion started: 23 August 2022

2.1 Algorithm for identifying rain steaks

Most existing algorithms aim to remove raindrops in images because raindrops are considered noise in object detection and tracking (Duthon et al., 2018). Such algorithms are categorized into multiple-image-based and single-image-based approaches (Jiang et al., 2018).

For example, Garg and Nayar (2007) classified the conditions in which the brightness difference between the previous pixel and that of the next pixel exceed a specific threshold over time, assuming that the background is fixed. Improved algorithms were then developed considering the temporal correlation of raindrops (Kim et al., 2015) and chromatic properties (Santhaseelan and Asari, 2015). Tripathi and Mukhopadhyay (2014) proposed a framework that removes rain that reduces the visibility of the scene to improve the detection performance of image feature information. However, single-image-based algorithms rely more on the properties of raindrops (Deng et al., 2018). The central idea of a single-image-based algorithm is to decompose rain-containing images into rainless layers (Li et al., 2016; Deng et al., 2018; Jiang et al., 2018).

An image including grayscale rainfall may be mathematically expressed in a two-dimensional (2D) matrix in which each element has a grayscale value. A single image (m×n) is expressed as follows (Jiang et al., 2018):

$$O = B + R, \tag{1}$$

where $O \in R^{m\times n}$, $B \in R^{m\times n}$, and $R \in R^{m\times n}$ are the raw image, rain-free background layer, and rain streak layer. Accordingly, various algorithms are available for rain streak identification. Different still image and video-based algorithms have been proposed to eliminate objects such as moving objects for application to actual surveillance cameras. However, most of these algorithms face optimization problems because of the vast number of decision variables (Jiang et al., 2019). This task is not easy to solve or requires excessive computation time. Therefore, existing studies present techniques suitable for post-analysis rather than application in real-time. The use of complex algorithms can increase versatility and accuracy, but there is a trade-off that reduces computational speed. The time required for such computing is a critical disadvantage in practical applications for estimating rainfall intensity.

In this study, a KNN-based segmentation algorithm (Zivkovic and Heijden, 2006), a popular non-parametrical method for background subtraction, was considered for segmenting the rain streaks (foreground) and background layers. KNN is used in classification and regression problems (Bouwmans et al., 2010). The concept of KNN is that similar things are close—the KNN-based segmentation algorithm finds the closest k samples (neighbors) to the unknown sample using Euclidean distance to determine the class (i.e., foreground or background). Thus, the KNN-based segmentation method to detect foreground changes in the video was used to identify rain streaks by recording infrared videos under conditions with little background influence. In the algorithm, The KNN subtractor works by updating the parameters of a Gaussian mixture model for more accurate kernel density estimation (Trnovszký et al., 2017). KNN is more efficient for local density estimation (Qasim et al., 2021); therefore, the algorithm is highly efficient if the number of foreground pixels is low.

https://doi.org/10.5194/amt-2022-196
Preprint. Discussion started: 23 August 2022

Atmospheric Measurement Techniques Discussions

We used the package provided by OpenCV to implement the KNN-based segmentation algorithm (Zivkovic and Heijden, 2006). Accordingly, three main parameters (history, dist2Threshold, detectShadows) needed to be set. Table 1 presents the description of the parameters used for the KNN background subtractor package.

Table 1: Parameters in KNN background subtractor package in OpenCV

Parameter	Description
history	Length of the history
dist2Threshold	Threshold on the squared distance between the pixel and the sample to decide whether a pixel is close to that sample. This parameter does not affect the background update.
detectShadows	If true, the algorithm will detect shadows and mark them. This decreases the speed slightly, so if you do not need this feature, set the parameter to false.

2.2 Estimation of DSD and rain rate

It is essential to capture raindrops within the camera's depth of field (DoF) to calculate the final DSD and rainfall intensity. Accordingly, this study proposed a novel algorithm to extract each rain streak from the rain streaks image. First, we applied a low-pass filter to the rain streaks image to remove unfocused raindrops that may remain in the image, which smooths each pixel using a 2D kernel. Highly detailed parts (e.g., out-of-focus raindrops and some noises) are erased, leaving some clear rain streaks. A background layer with a value of 0 and a part not in the image were separated to extract the rain streaks and labeled one by one to identify each rain streak from the image.

Because the rain streak observed in the surveillance camera image causes an angle difference (influenced by the wind), a diameter estimation process considering the angle of the rain streak (fall angle of a raindrop) is required. If the angle of rain steak is considered and converted to the raindrop diameter through the horizontal pixel size in the image, the shape change in the raindrop because of air buoyancy (i.e., during the falling of the raindrop) may not be reflected, and overestimation can occur.

Accordingly, the representative angle of each extracted rain streak was calculated. The border information of each rain streak was obtained, and center axis information of the rain streak was obtained based on the border information to calculate the drop angle. Moreover, the rain streak was rotated to set the long and short axes of the streak at 0° and 90°, using the angle information.

The size of raindrops in the rain streaks image can be estimated through the analysis of microphysical characteristics of raindrop and geometric optical analysis (Keating, 2002). The instantaneous velocity of a raindrop on the ground can be estimated from the exposure time and the size of the raindrop. However, the distance from the raindrop to the lens surface (i.e., the object distance) is unknown and should be inferred. Object distance can be calculated through physical optics analysis because it causes perspective distortion. Assuming a raindrop is spherical, the length of the trajectory where the

https://doi.org/10.5194/amt-2022-196
Preprint. Discussion started: 23 August 2022

Atmospheric Measurement Techniques Discussions

raindrop falls when the camera is exposed and the diameter of the raindrop can be inferred through the lens equation (Keating, 2002):

$$L(s) = \frac{d_f - f}{d_f \cdot f} \frac{h_s}{h_p} l_p s, \tag{2}$$

$$D(s) = \frac{d_f - f}{d_f \cdot f} \frac{w_s}{w_p} d_p s, \tag{3}$$

where s is the distance from the raindrop to the lens plane (mm). $L(s)$ and $D(s)$ are the length of falling trajectory during camera exposure (rain streak) and the raindrop's diameter. d_f is the focus distance (mm), f is focal length (mm). h_s and w_s are the vertical and horizontal sizes of the active area of the image sensor (mm), and h_p and w_p are the vertical and horizontal sizes of the captured image (in number of pixels). l_p and d_p are the length and width of the rain streaks in the image (in number of pixels).

It is then possible to infer the falling speed of raindrops using the camera's exposure time (Jiang et al., 2019), as follows:

$$v(s) = \frac{L(s)}{1000\tau}, \tag{4}$$

where τ is the exposure time of the camera (seconds) and $v(s)$ is the fall velocity of the raindrop from the image. Furthermore, the fall velocity of a raindrop can be approximated by an empirical formula for raindrop diameter. The most frequently used equation is as follows (Atlas et al., 1973; Friedrich et al., 2013):

$$v(D) = 9.65 - 10.3\exp(-0.6D), \tag{5}$$

where D is the raindrop diameter and v is the fall velocity of raindrop. The actual diameter of raindrops can be obtained by solving the equation with the fall velocity obtained through the exposure time and Eqs. (4) and (5). Furthermore, the DoF for the images using the camera's setting information can be calculated, and the effective volume for estimating rainfall intensity can be obtained. Details of the process are described in previous studies (Allamano et al., 2015; Jiang et al., 2019).

The control volume must be determined to estimate the rainfall intensity using the diameter of each raindrop. An understanding of DoF is required to achieve the volume. The DoF, is simply the range at which the camera can accurately focus and capture the raindrops. Calculating this range requires obtaining the near and far focus planes as follows:

$$s_n = \frac{d_f \cdot f^2}{f^2 + N \cdot c_p \cdot (d_f - f)}, \tag{6}$$

$$s_f = \frac{d_f \cdot f^2}{f^2 - N \cdot c_p \cdot (d_f - f)}, \tag{7}$$

where s_n and s_f are the distances from the near and far focus planes. c_p is the maximum permissible circle of confusion, a constant determined by the camera manufacturers. N is the F-number of the lens relevant to the aperture diameter. Accordingly, the theoretical sampling volume (V, m^3) indicate the truncated rectangular pyramid between the near and far focus planes:

https://doi.org/10.5194/amt-2022-196
Preprint. Discussion started: 23 August 2022

Atmospheric Measurement Techniques Discussions

$$V = \frac{1}{3\cdot 10^9}\left(\frac{d_f - f}{d_f \cdot f}\right)^2 w_s h_s (s_f^3 - s_n^3), \tag{8}$$

Then, we used the gamma distribution equation, Eq. (6), proposed by Ulbrich (1983), to calculate DSD parameters using data at every 1 min interval.

$$N(D) = N_0 D^{\mu} \exp(-\Lambda D), \tag{9}$$

where $N(D)$ ($mm^{-1}m^{-3}$) is the number concentration value per unit volume for each size channel, and N_0 ($mm^{-1-\mu}m^{-3}$) is an intercept parameter representing the number concentration when the diameter has 0 value. D (mm) and Λ (mm^{-1}) are the drop diameter (mm) and slope parameter. Raindrops smaller than 8.0 mm were used to avoid considering non-weather data such as leaps and bugs (Friedrich et al., 2013).

The gamma distribution relationship is a function of formulating the number concentration per unit diameter and unit volume. It was proposed by Marshall and Palmer (1948) as improved model of exponential distribution as a favorable form to reflect various rainfall characteristics. By including the term containing μ in the distribution function, the shape of the number concentration distribution for small drops smaller than 1 mm is improved.

$$N(D) = N_0 \exp(-\Lambda D), \tag{10}$$

As the Λ decreases, the slope of the distribution shape decreases and the proportion of large drop increases. Conversely, as the value increases, the distribution slope becomes steeper, and the weight of the large particles decreases. When μ has a large value, the distribution is convex upward, and it has a distribution with a sharp decrease in number concentration at small diameters. Whereas when it has a negative value, the distribution is convex downward with an increase in the concentration of drops smaller than 1 mm. In the gamma distribution, the μ is mainly affected by the difference in concentration of raindrops smaller than 3 mm (Vivekanandan et al., 2004).

Vivekanandan et al. (2004) explained the reason for using the gamma distribution as follows. First, it is sufficient to calculate the rainfall estimation equation using only the first, third, and fourth moments (Eq. (11)) (Smith, 2003). Second, the long-term raindrop size distribution has an exponential distribution shape (Yuter and Houze, 1997).

The raindrop size distribution observed from the ground is the result of the microphysical development of raindrops falling from precipitation clouds. The drop size distribution shape is changed during fall by microphysical processes such as collision, merging, and evaporation, and changes in the concentration of drops larger than 7.5 mm and small drops occur mainly. As a result, the drop size distribution observed on the ground mainly follows the gamma distribution shape (Ulbrich, 1983; Tokay and Short, 1996). The gamma distribution relationship should be used to analyze the distribution of raindrops that are actually floating and falling.

$$M_n = \int_{D_{min}}^{D_{max}} D^n N(D) dD, \tag{11}$$

https://doi.org/10.5194/amt-2022-196
Preprint. Discussion started: 23 August 2022

Eq. (11) indicate a moment expression for the n^{th} order. For example, the second moment is calculated as the product of the square of the diameter of each channel and the number concentration and the diameter of each channel. Each moment value has a different microphysical meaning. Therefore, the gamma distribution including three dependent parameters is more advantageous in reflecting the microphysical characteristics of the precipitation system than the exponential distribution including two dependent parameters. Eq. (11) can be expressed in gamma distribution format as follows:

$$M_n = \int_{D_{min}}^{D_{max}} D^n N(D) dD = N_0 \Lambda^{-(\mu+n+1)} \Gamma(\mu + n + 1), \tag{12}$$

where N_T (total number concentration, m^{-3}) is the zero-order moment (M_0) and represents the total number concentration of raindrops per unit volume. η was determined for calculating μ and Λ. In this study, a combination of moments in the ratio of M_2, M_4, and M_6, which accurately represents the characteristics of small rainfall particles, was applied (Vivekanandan et al., 2004):

$$\eta = \frac{\langle M_4 \rangle^2}{\langle M_2 \rangle \langle M_6 \rangle} = \frac{(\mu+3)(\mu+4)}{(\mu+5)(\mu+6)}, \tag{13}$$

μ and Λ are calculated as follows:

$$\mu = \frac{(7-11\eta) - \left[(7-11\eta)^2 - 4(\eta-1)(30\eta-12)\right]^{1/2}}{2(\eta-1)}, \tag{14}$$

$$\Lambda = \left[\frac{M_2 \Gamma(\mu+5)}{M_4 \Gamma(\mu+3)}\right]^{1/2} = \left[\frac{M_2(\mu+4)(\mu+3)}{M_4}\right]^{1/2}, \tag{15}$$

A larger value of D_m (mm) estimated using Eq. (16), the diameter of the average mass of raindrops contained in the unit volume, indicates that predominantly larger drops are distributed.

$$D_m = \frac{M_4}{M_3}, \tag{16}$$

R (mm h^{-1}) is the rain rate calculated using Eq. (17).

$$R = \frac{6\pi}{10^4} \int_{D_{min}}^{D_{max}} D^3 N(D) V(D) dD, \tag{17}$$

3 Study site and observation equipment

This study used a building's rooftop as the study site. The building is the Chung-Ang University's Bobst Hall, located in the central region of Seoul in Korea. It is located at 37° 30' 13" north latitude and 126° 57' 27" east longitude, at an elevation of 42 m. Fig. 2 illustrates the CCTV (marked with a red circle) and PARSIVEL installed at the study point. The CCTV was used for the main analysis, and PARSIVEL was considered for verification purposes.

https://doi.org/10.5194/amt-2022-196
Preprint. Discussion started: 23 August 2022

(a) Surveillance camera (b) PARSIVEL

Figure 2: Observation measurements considered in this study

The CCTV model used in this study is DC-T333CHRX, developed by IDIS. The camera has a 1/1.7 inch complementary metal-oxide semiconductor (CMOS) with a height and width of 5.70 mm and 7.60 mm. The focal length is 4.5 mm, and the F-number of the lens is 1.6. The shutter speed was set to 1/250 s, and the frame per second (fps) was set to 30. The infrared ray distance is 50 m. The maximum permissible circle of confusion is 0.005 mm. The camera's resolution is 1,080 pixels for the height and 1,920 pixels for the width, but the cropped images (640×640 pixels) were considered for the analysis.

The PARSIVEL is a ground meteorological instrument that can observe precipitation particles' diameter and fall speed (e.g., raindrops, snow particles, hail) (Löffler–Mang and Joss, 2000). The meteorological information, including raindrop size, is used to estimate the quantitative precipitation amount and reveal the precipitation system's microphysical characteristics and development mechanism.

The PARSIVEL used in this study is the second version of the instrument manufactured by OTT in Germany, and it is improved observation accuracy of small particles. The PARSIVEL uses a laser-based optical sensor to send a laser from the transmitter and continuously receive it from the receiver (Fig. 3). As the laser beam moves from the transmitter to the receiver, the precipitation particle passes over the laser beam, and the size and velocity of the precipitation particle are observed (Nemeth and Hahn, 2005). The diameter and velocity of the particle are calculated by calculating the time the particle passes through the laser and the laser intensity that decreases during the passage (Fig. 4).

https://doi.org/10.5194/amt-2022-196
Preprint. Discussion started: 23 August 2022

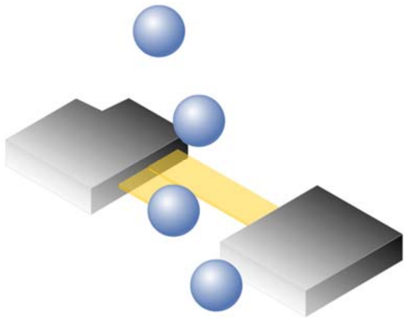

Figure 3: Functional principle of the PARSIVEL disdrometer.

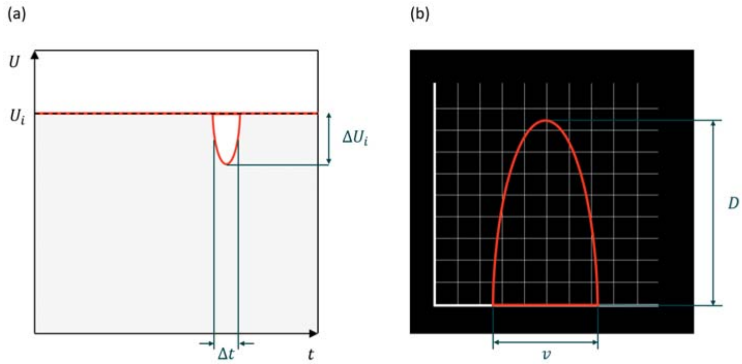

Figure 4: (a) Signal changes whenever a particle falls through the beam anywhere within the measurement area. (b) The degree of dimming is a measure of the particle's size; together with the duration of the signal, the fall velocity can be derived.

Parameters such as rain rate, reflectivity, and momentum of raindrops are calculated through particle concentration values for each diameter and falling speed channel obtained through PARSIVEL observation. In this study, the temporal resolution of the observation data was set to 1 minute. The particle diameters from 0.2 to 25 mm (Table 2) and fall velocity from 0.2 to 20 m s^{-1} (Table 3) can be observed by the PARSIVEL. The particle diameter and the fall speed each have 32 observation channels, so the number of observed particles for the time resolution set in 1,024 channels (32×32) is observed. The first and second channels of diameter are not included in the observable range of the PARSIVEL and are treated as noise. Therefore, the observation data of the first and second diameter channels were not considered in the actual analysis. The detailed information on the specifications of the PARSIVEL is presented in Table 4.

https://doi.org/10.5194/amt-2022-196
Preprint. Discussion started: 23 August 2022

Table 2: The representative diameter and spread for each diameter channel class.

Class number	Class average (mm)	Class spread (mm)	Class number	Class average (mm)	Class spread in (mm)
1	0.062	0.125	17	3.250	0.500
2	0.187	0.125	18	3.750	0.500
3	0.312	0.125	19	4.250	0.500
4	0.437	0.125	20	4.750	0.500
5	0.562	0.125	21	5.500	1.000
6	0.687	0.125	22	6.500	1.000
7	0.812	0.125	23	7.500	1.000
8	0.937	0.125	24	8.500	1.000
9	1.062	0.125	25	9.500	1.000
10	1.187	0.125	26	11.000	2.000
11	1.375	0.250	27	13.000	2.000
12	1.625	0.250	28	15.000	2.000
13	1.875	0.250	29	17.000	2.000
14	2.125	0.250	30	19.000	2.000
15	2.375	0.250	31	21.500	3.000
16	2.750	0.500	32	24.500	3.000

Table 3: The representative fall velocity and spread for each diameter channel class.

Class number	Class average (m s^{-1})	Class spread (m s^{-1})	Class number	Class average (m s^{-1})	Class spread (m s^{-1})
1	0.050	0.100	17	2.600	0.400
2	0.150	0.100	18	3.000	0.400
3	0.250	0.100	19	3.400	0.400
4	0.350	0.100	20	3.800	0.400
5	0.450	0.100	21	4.400	0.800
6	0.550	0.100	22	5.200	0.800
7	0.650	0.100	23	6.000	0.800
8	0.750	0.100	24	6.800	0.800
9	0.850	0.100	25	7.600	0.800
10	0.950	0.100	26	8.800	1.600
11	1.100	0.200	27	10.400	1.600
12	1.300	0.200	28	12.000	1.600
13	1.500	0.200	29	13.600	1.600
14	1.700	0.200	30	15.200	1.600
15	1.900	0.200	31	17.600	3.200
16	2.200	0.400	32	20.800	3.200

https://doi.org/10.5194/amt-2022-196
Preprint. Discussion started: 23 August 2022

Atmospheric Measurement Techniques
Discussions

Table 4: Technical information of the PARSIVEL disdrometer.

		Technical information
Wavelength of optical sensor		780 nm
Measuring area		30 × 180 mm (54 cm^2)
Measuring range	Size	0.2 ~ 25 mm (32 channel class)
	Fall velocity	0.2 ~ 20 m s^{-1} (32 channel class)
Precipitation intensity		0.001 ~ 1,200 mm h^{-1}
Measurement time interval		10 sec ~ 60 min
Instrument dimensions (H×W×D)		670 × 600 × 114 mm

4 Application result

4.1 Rainfall event

We considered a rainfall event from 1945 LST on March 25, 2022, to 0615 LST on March 26, 2022. Fig. 5 illustrates the hyetographs of the rainfall event considered in this study according to the time resolution. The total rainfall is 18.6 mm based on the PARSIVEL. The maximum rain rate is 9.9 mm h^{-1} based on the 1 min resolution and 1.1 mm h^{-1} based on the 15 min resolution.

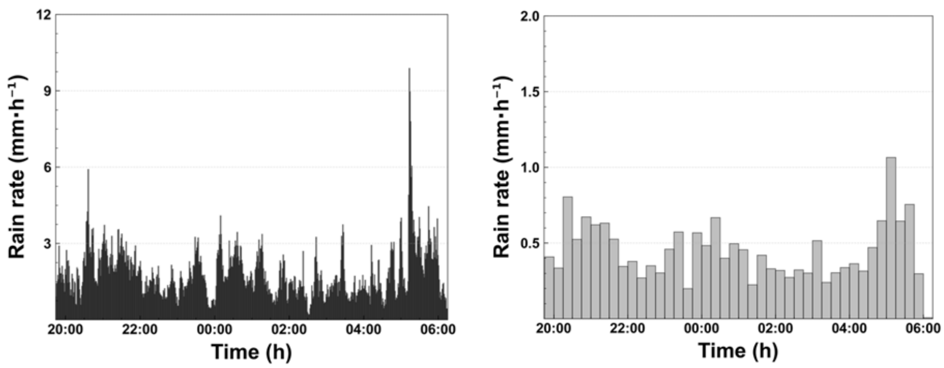

(a) 1 min (b) 15 min

Figure 5: Hyetograph of PARSIVEL and rain gauge observation data for the rainfall event considered in this study

https://doi.org/10.5194/amt-2022-196
Preprint. Discussion started: 23 August 2022

Atmospheric Measurement Techniques Discussions

4.2 Identifying rainfall streaks

The rain streaks were distinguished from the original raw images using the KNN-based algorithm described in Section 2.1. Accordingly, two parameters (history and dist2Threshold) were set to default values (500 and 400). The other parameter (detectShadows) was set to "false." Fig. 6 illustrates the raw, background, and rain streaks images for an example time image (20:30:57 March 25, 2022), scaled in yellow to make it easier to verify the visual change.

(a) Raw image (b) Background image (c) Rain streaks image

Figure 6: Segmentation example of raw image into background and rain streaks image based on KNN-based algorithm (20:30:57 March 25, 2022)

As confirmed in Fig. 6, adequate background separation performance can be achieved using the KNN-based method used in this study. Because it is an infrared camera and the camera's exposure time is 1/250 s, the length of rain streaks is relatively short. The longer the exposure time, the longer the raindrops appear on the image (Schmidt et al., 2012; Allamano et al., 2015). If the exposure time is too long, some rain streaks may penetrate the image. In this case, it is difficult to estimate the rain streak length, a clue for estimating raindrop size.

The identification algorithm was implemented using Anaconda Software Distribution on a workstation with an AMD Ryzen 5 5600X 6-Core Processor and 32 GB RAM. The computing time for the 15 min video was approximately 50 s using only CPU computation. As described previously, the KNN-based algorithm used in this study has high-speed computing performance compared with various algorithms based on optimization, so it will likely have an advantage in real-time applications.

4.3 Estimation of DSD and rain rate

The rain streaks image presented in Fig. 6(c) was not considered for the final DSD estimation because of noise and factors other than rain caused by the sudden brightness change. As described in Section 3, a low-pass filter was first applied rain streaks image.

https://doi.org/10.5194/amt-2022-196
Preprint. Discussion started: 23 August 2022

The 10×10 kernel was applied considering the total image size (640×640), and each grid value of the kernel was set to 0.01. The set kernel was filtered by convolution pixel by pixel. Moreover, the convolution was performed once more using the following 2D kernel [0 1 0; -1 0 1; 0 -1 0] to highlight the rim of the rain streaks. A background layer with a value of 0 and a part not in the image were separated to extract the rain streaks, which were labeled one by one to identify each rain streak from the image. Fig. 7(a) illustrates the example result after performing the processes described above to Fig. 6(c). Each rain streak was then separated and labeled, as in Fig. 7(b).

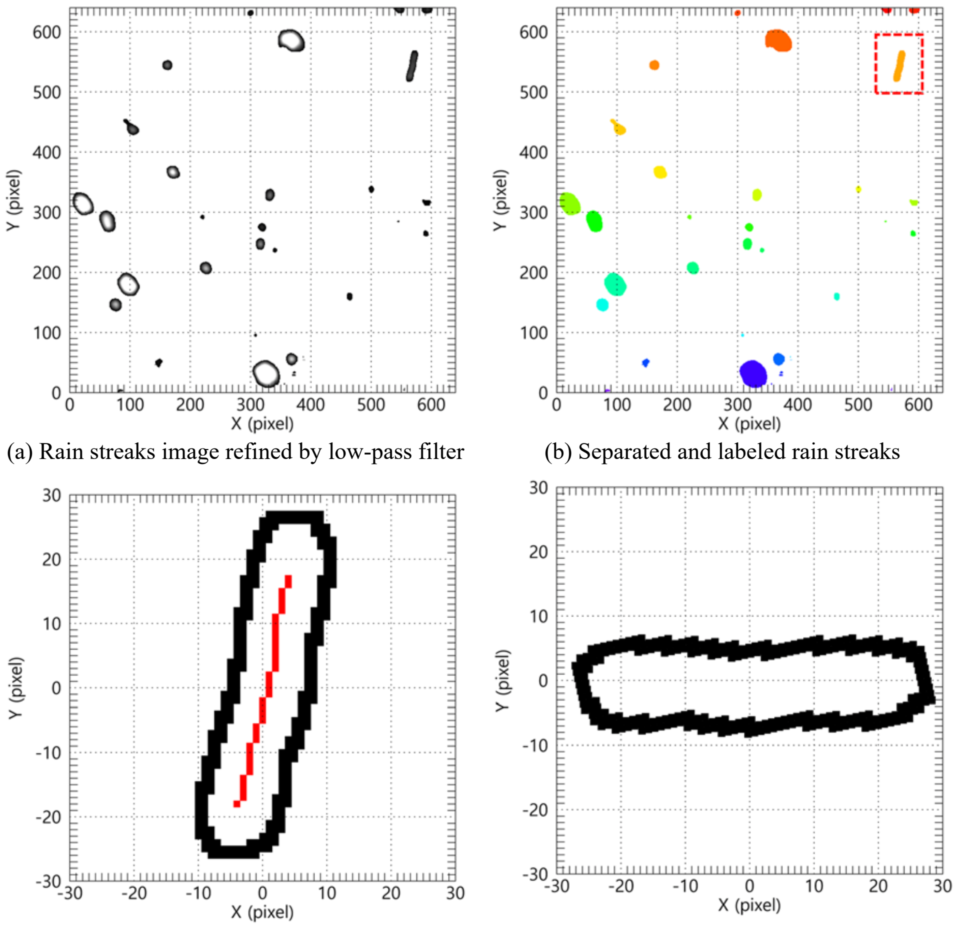

(a) Rain streaks image refined by low-pass filter

(b) Separated and labeled rain streaks

(c) Center axis for a rain streak

(d) Rotated rain streak considering canting angle

Figure 7. Extraction example of rain streak based on the proposed algorithm

https://doi.org/10.5194/amt-2022-196
Preprint. Discussion started: 23 August 2022

The border information of each rain streak needed to be obtained. The center axis was calculated by connecting the center (median) of the minimum pixel and maximum pixel values of the x-axis for each y-axis using border information. The angle of rain steak was obtained from the slope value obtained by calculating the linear function through the center axis's x and y pixel number values. Fig. 7(c) is an example of the extraction of a rain streak extracted from the image of Fig. 7(b).

The drop angle was then calculated, and the rain streak was rotated using the angle information. Raindrops can be broken up by strong wind or collisions between raindrops during falling. The maximum difference value between the minimum and maximum pixel number values of y-axis calculated using border information of the rotated rain steak was used to calculate the raindrop diameter and exclude the influence of the distorted shape of rain steak by break up (Fig. 7d) (Testik, 2009; Testik and Pei, 2017). Fig. 7(d) illustrates the result of the final process.

Fig. 8 illustrates the time series of the number concentration and D_m obtained from CCTV and PARSIVEL. From 1945 LST to 2350 LST, the maximum number concentration of lower than 1,000 $mm^{-1}m^{3}$ was observed from the PARSIVEL observation, and from 2000 LST to 2010 LST, a number concentration lower than 100 $mm^{-1}m^{-3}$ was observed. At 2005 LST, large raindrops (of 3.8 mm) were observed, resulting in a sharp increase in Dm above 2 mm. In contrast, in the results based on CCTV images, the number concentration of less than 10,000 $mm^{-1}m^{-3}$ was continuously demonstrated during the entire analysis period, and a number concentration greater than 5,000 $mm^{-1}m^{-3}$ was observed before 2200 LST. Because the proportion of small drops was high, D_m was predominantly less than 1.5 mm.

From 0000 LST to 0100 LST, both CCTV and PARSIVEL-based data had a predominant maximum diameter of about 2.4 mm. At 0035 LST, raindrops larger than 3.2 mm were observed in PARSIVEL, but raindrops less than 3 mm were not observed in CCTV. However, the number concentration of small diameters of 0.5 mm or less had similar values between 1,000 and 5,000 $mm^{-1}m^{3}$. Despite the difference in the maximum size of the drops, there was no predominant difference in the Dm because the number concentration of raindrops smaller than 1 mm had similar values.

From 0300 LST to 0530 LST, number concentrations higher than 5,000 $mm^{-1}m^{-3}$ in the raindrops smaller than 1 mm were observed using PARSIVEL. However, CCTV data revealed that number concentrations less than 5,000 $mm^{-1}m^{-3}$ were consistently observed. At 1714 LST, raindrops of up to 3.2 mm were observed through PARSIVEL, but the maximum diameter was overestimated to be greater than 3.5 mm based on CCTV. In CCTV images, the D_m was close to 3 mm because of the overestimation of diameter and underestimation of number concentration for raindrops less than 1 mm. There was a difference with the D_m value obtained through PARSIVEL observation.

https://doi.org/10.5194/amt-2022-196
Preprint. Discussion started: 23 August 2022

Atmospheric Measurement Techniques Discussions
Open Access

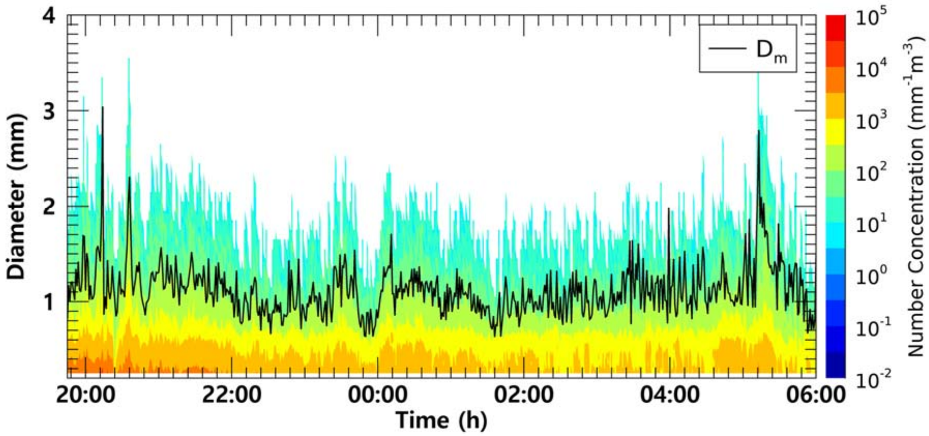

(a) CCTV

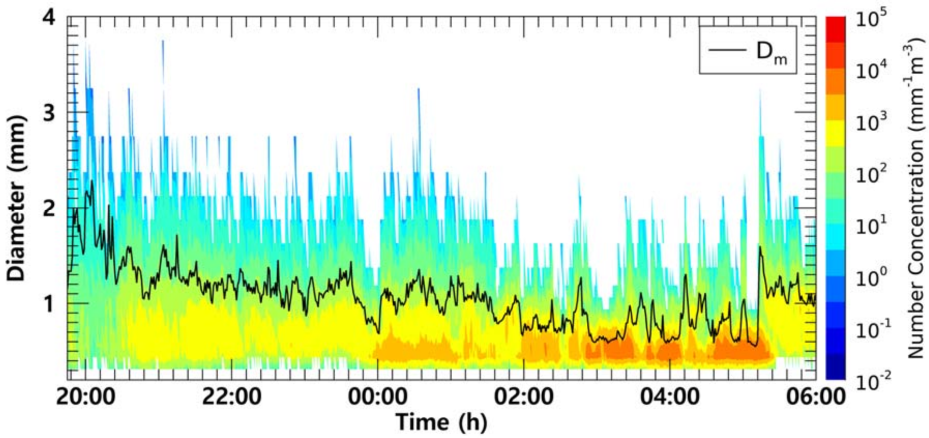

(b) PARSIVEL

Figure 8: Time series of number concentration and Dm (black coloured line) from (a) the surveillance camera images, (b) the PARSIVEL observation data from 2145 LST on March 25 to 0600 LST on March 26, 2022.

Fig. 9 illustrates the average number concentration versus diameter of raindrops calculated using CCTV image and PARSIVEL observation data from 1945 LST on March 25 to 0600 LST on March 26, 2022. The PARSIVEL disdrometer data has a fixed raindrop diameter channel; thus, it can differ in number concentration depending on the diameter channel setting. Therefore, in this study, the simulated DSD through the gamma model was also analyzed to compare the distribution of rainfall particles.

https://doi.org/10.5194/amt-2022-196
Preprint. Discussion started: 23 August 2022

Atmospheric Measurement Techniques
Discussions

For raindrop diameters from 0.7 to 1.5 mm, the simulated and observed number concentrations produced similar values. However, above 1.5 mm, the model-based number concentration was under-simulated. From these results, in the precipitation cases selected in this study, the gamma model appears limited in simulating the number concentration of raindrops larger than 3 mm. In diameters from 0.5 to 1.5 mm, the number concentration obtained from CCTV images tended to be lower than that from PARSIVEL observation and higher in diameters above 1.5 mm. PARSIVEL observation data decreased sharply for diameters smaller than 0.3 mm. In contrast, CCTV gradually increased the number concentration as the diameter decreased.

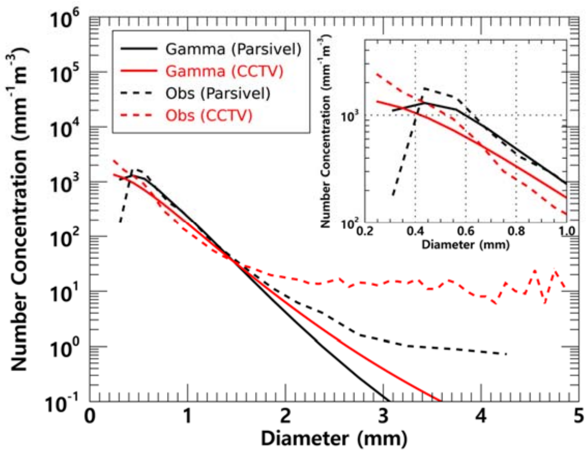

Figure 9: Average number concentration versus diameter from the surveillance camera images and the PARSIVEL.

Rainfall intensity was estimated based on the obtained number concentration from CCTV images and PARSIVEL. The near (s_n) and far (s_f) focus planes were calculated as 718 and 1,648 mm from Eqs. (8) and (9). The DoF was calculated as 930 mm. The focal distance was set to 1 m, referring to previous studies (Dong et al., 2017; Jiang et al., 2019). The control volume was 2.9 m^{-3}, applying Eq. (10) with the variables determined above. Fig. 10 illustrates the rain rate time series calculated using CCTV images and PARSIVEL observation data. The increase or decrease in rain rate according to time change based on CCTV data followed the trend of rainfall intensity change based on PARSIVEL observation data.

At 0400 LST and 0516 LST, PARSIVEL observation data revealed rain rates of up to 1.5 mm h^{-1} and 9.8 mm h^{-1}, but CCTV image-based rain rates were overestimated to be larger than 3.5 mm h^{-1} and 15 mm h^{-1}. During the period where the difference in rain rate is large, compared with the PARSIVEL observation data, relatively larger raindrops were applied to the rain rate calculation, resulting in an error. At 2014 LST on March 25 and at 0516 LST on March 26, raindrops larger than 3.5 mm were considered in the rain rate calculation, which increased the rain rate error.

https://doi.org/10.5194/amt-2022-196
Preprint. Discussion started: 23 August 2022

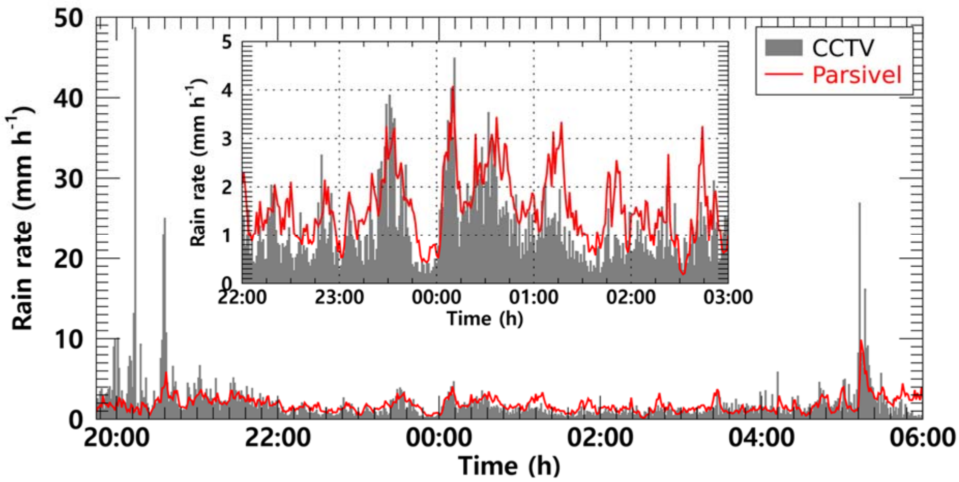

Figure 10: The rain rate time series calculated from the surveillance camera images (gray bar) and PARSIVEL observation data (red line) from 2145 LST on March 25 to 0600 LST on March 26, 2022.

Fig. 11 illustrates the scatter plot of the average rain rate every 15 min from the PARSIVEL observation and the CCTV images. Uncertainty exists in the resolution of the rain gauge in the 1 min step. Accordingly, the time step for analysis is set to 15 min. The slope of the rainfall intensity was close to 1 except for the period when the rain rate was overestimated by the raindrops larger than 3 mm. During the entire analysis time, the rain rate slope was 1.33, revealing that the error increased with rainfall intensity.

The cumulative average rainfall intensity every 15 min was weaker than 10 mm h^{-1}, concentrated at a rain rate less than 4 mm h^{-1}, so the correlation coefficient (CC) was 0.58. Furthermore, the mean absolute error (MAE), root mean square error (RMSE), and mean absolute percent error (MAPE) were 0.84 mm h^{-1}, 1.43 mm h^{-1}, and 44%. Differences according to rain rate can also be determined. The accuracy is higher at a rain rate smaller than 2 mm h^{-1} as a boundary. The MAE, RMSE, and MAPE were 0.32 mm h^{-1}, 0.67 mm h^{-1}, and 32% for a rain rate of 2 mm h^{-1} or less, and 1.49 mm h^{-1}, 2.37 mm h^{-1}, and 73% for a rain rate above 2 mm h^{-1}.

The statistical values of the rain rate and DSD parameters for the rainfall cases analyzed in this study are summarized in Table 5. The rain rate and D_m calculated using CCTV images were 0.16 mm h^{-1} and 0.05 mm more than the values calculated using PARSIVEL observation data on average, respectively. A high rain rate and D_m were caused by overestimating the number concentration for raindrops larger than 1.5 mm confirmed in Fig. 9. The number concentration for the small diameter (less than 0.3 mm) was higher in the CCTV data than in the PARSIVEL data.

However, the rain rate was not significantly affected by small raindrops. Although D_m calculated from the PARSIVEL observation data had a low value (1.061 mm), the CCTV data revealed a high skewness (of 1.793) because of the high

https://doi.org/10.5194/amt-2022-196
Preprint. Discussion started: 23 August 2022

number concentration for raindrops smaller than 0.1 mm. the high kurtosis (104.945 and 7.849) for the rain rate and D_m of the CCTV-based data were caused by the overestimated number concentration of 1.5 mm or larger. Moreover, as the distribution spread widely, μ was as low as 1.312. Because of the high number concentration for raindrops larger than 3 mm of CCTV, the PARSIVEL observation data had a Λ value of 9.982 mm^{-1}, whereas the CCTV data had a low value (5.187 mm^{-1}).

Table 5: Statistical values of the rain rate and DSD parameters for the rainfall case in this study.

		R (mm h^{-1})	D_m (mm)	$Log_{10}N_0$ (mm$^{-1-\mu}$m^{-3})	μ (unitless)	Λ (mm^{-1})
PARSIVEL	Mean	1.829	1.061	6.583	5.103	9.982
	Variance	1.013	0.088	11.768	24.124	69.899
	Skewness	2.341	0.814	2.447	2.11	2.687
	Kurtosis	12.295	1.562	7.226	5.335	8.54
CCTV	Mean	1.994	1.116	4.405	1.312	5.187
	Variance	9.274	0.07	0.422	0.913	3.527
	Skewness	8.528	1.793	1.427	1.075	1.441
	Kurtosis	104.945	7.849	2.731	1.664	2.802

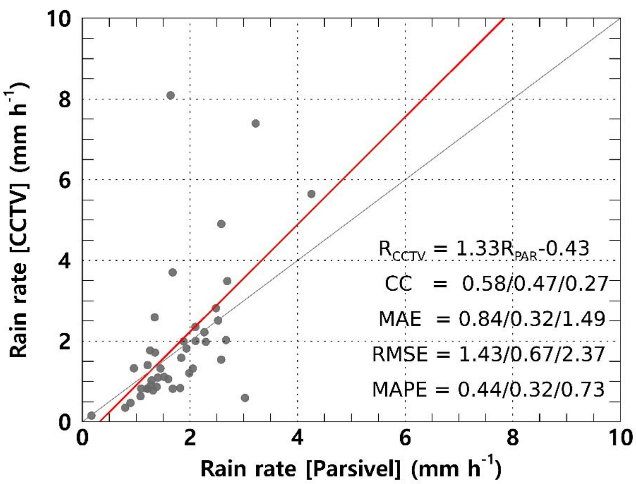

https://doi.org/10.5194/amt-2022-196
Preprint. Discussion started: 23 August 2022

Fig. 11. Scatter plot of average rain rate every 15 minutes from the PARSIVEL observation and the surveillance camera images. Red line is linear regression. Scatter plot displays CC, MAE, RMSE, MAPE for R > 0 mm h^{-1}, R < 2 mm h^{-1}, and R ≥ 2 mm h^{-1} (sequentially from left to right).

6 Conclusion

This study estimated DSD with an infrared surveillance camera, based on which rainfall intensity was also estimated. Rain streaks were extracted using a KNN-based algorithm. The rainfall intensity was estimated based on DSD using physical optics analysis. A rainfall event was selected, and the applicability of the method in this study was examined. The estimated DSD was verified using a PARSIVEL. Furthermore, a tipping-bucket rain gauge was used for comparison. The results from this study can be summarized as follows.

KNN-based algorithm illustrates suitable performance in separating the rain streaks and background layers. Furthermore, the possibility of separation for each rain streak and estimation of DSD was sufficient.

The number concentration of raindrops obtained through the CCTV images was similar to the actual PARSIVEL observed number concentration in the 0.5 to 1.5 mm section. In the small raindrops in the section of 0.4 mm or less, the PARSIVEL observation data underestimates the actual DSD. However, the CCTV image-based rain rate had an advantage over the raindrop-based data—the number concentration decreased rapidly as the number concentration gradually increased in the 0.2–0.3 mm diameter section.

The maximum raindrop diameter and number concentration of less than 1 mm produced similar results during the period with a high ratio of diameters less than 3 mm. However, the number concentration was overestimated during the period when raindrops larger than 3 mm were observed. The CCTV image-based data revealed that the rain rate was overestimated because of the overestimation of raindrops larger than 3 mm. After comparing with the 15-min cumulative PARSIVEL rain rate, the CCs—MAE, RMSE, and MAPE—were 0.84 mm h^{-1}, 1.43 mm h^{-1}, and 44%. The differences according to rain rate can be identified. The accuracy is higher at a rain rate smaller than 2 mm h^{-1} as a boundary.

The rain rate and Dm calculated using CCTV images exhibited similar average values. The overestimated number concentration of 1.5 mm or larger caused high kurtosis for the rain rate and D_m of CCTV-based data and a low μ value. Because of the high number concentration for raindrops larger than 3 mm of CCTV, the PARSIVEL observation data had a higher Λ value than the result based on the CCTV data.

In this study, DSD was estimated using an infrared surveillance camera; the rain rate was also estimated. Consequently, we could confirm the possibility of estimating an image-based DSD and rain rate obtained based on low-cost equipment in dark conditions.

https://doi.org/10.5194/amt-2022-196
Preprint. Discussion started: 23 August 2022

Atmospheric Measurement Techniques Discussions

Acknowledgements

This research was supported by the Korea Meteorological Administration Research and Development Program (KMI2022-01910) and Basic Science Research Program through the National Research Foundation of Korea (NRF) funded by the Ministry of Education (2022R1I1A1A01065554).

References

Allamano, P., Croci, A., Laio, F.: Toward the camera rain gauge. Water Resour. Res. 51 (3), 1744-1757, 2015

Atlas, D., Srivastava, R. C., Sekhon, R. S.: Doppler radar characteristics of precipitation at vertical incidence. Rev. Geophys. 11 (1), 1–35, 1973.

Avanzato, R., Beritelli, F.: A cnn-based differential image processing approach for rainfall classification. Adv. Sci. Technol. Eng. Syst. J. 5 (4), 438-444, 2020.

Bouwmans, T., El Baf, F., Vachon, B.: Statistical background modeling for foreground detection: A survey. In: Chen, C. H. (Ed.) Handbook of pattern recognition and computer vision, fourth ed. World Scientific, Singapore, pp. 181-199, 2010

Cai, F., Lu, W., Shi, W., He, S.: A mobile device-based imaging spectrometer for environmental monitoring by attaching a lightweight small module to a commercial digital camera. Sci. Rep. 7 (1), 1-9, 2017.

Deng, L. J., Huang, T. Z., Zhao, X. L., Jiang, T. X.: A directional global sparse model for single image rain removal. Appl. Math. Model. 59, 662.679, 2018.

Dong, R., Liao, J., Li, B., Zhou, H., Crookes, D.: Measurements of rainfall rates from videos. In 2017 10th International Congress on Image and Signal Processing, BioMedical Engineering and Informatics, IEEE, Shanghai, China, 14-16 October, pp. 1-9, 2017.

Duthon, P., Bernardin, F., Chausse, F., Colomb, M.: Benchmark for the robustness of image features in rainy conditions. Mach. Vis. Appl. 29 (5), 915.927, 2018.

Famiglietti, J. S., Cazenave, A., Eicker, A., Reager, J. T., Rodell, M., Velicogna, I.: Satellites provide the big picture. Sci. 349 (6249), 684-685, 2015.

Friedrich, K., Kalina, E. A., Masters, F. J., Lopez, C. R.: Drop-size distributions in thunderstorms measured by optical disdrometers during VORTEX2. Mon. Weather Rev. 141 (4), 1182-1203, 2013.

Garg, K., Nayar, S. K.: Vision and rain. Int. J. Comput. Vis. 75 (1), 3-27, 2007.

Guo, B., Han, Q., Chen, H., Shangguan, L., Zhou, Z., Yu, Z.: The emergence of visual crowdsensing: Challenges and opportunities. IEEE Commun. Surv. Tutor. 19 (4), 2526-2543, 2017.

Guo, H., Huang, H., Sun, Y. E., Zhang, Y., Chen, S., Huang, L.: Chaac: Real-time and fine-grained rain detection and measurement using smartphones. IEEE Internet Things J. 6 (1), 997-1009, 2019

Haberlandt, U., Sester, M.: Areal rainfall estimation using moving cars as rain gauges-A modelling study. Hydrol. Earth Syst. Sci. 14 (7), 1139-1151, 2010.

https://doi.org/10.5194/amt-2022-196
Preprint. Discussion started: 23 August 2022

Atmospheric Measurement Techniques
Discussions

Hua, X. S.: The city brain: Towards real-time search for the real-world. In The 41st International ACM SIGIR Conference on Research & Development in Information Retrieval, New York, NY, 8-12 July. pp. 1343-1344, 2018

Jiang, S., Babovic, V., Zheng, Y., Xiong, J.: Advancing opportunistic sensing in hydrology: A novel approach to measuring rainfall with ordinary surveillance cameras. Water Resour. Res. 55 (4), 3004-3027, 2019.

Jiang, T. X., Huang, T. Z., Zhao, X. L., Deng, L. J., Wang, Y.: Fastderain: A novel video rain streak removal method using directional gradient priors. IEEE Trans. Image Process. 28 (4), 2089-2102, 2018.

Kathiravelu, G., Lucke, T., Nichols, P.: Rain drop measurement techniques: A review. Water, 8 (1), 29, 2016.

Keating, M. P.: Geometric, physical, and visual optics, Second ed. Butterworth-Heinemann, Oxford, UK, 2002.

Kidd, C., Becker, A., Huffman, G. J., Muller, C. L., Joe, P., Skofronick-Jackson, G., Kirschbaum, D. B.: So, how much of the Earth's surface is covered by rain gauges?. Bull. Am. Meteorol. Soc. 98 (1), 69-78, 2017.

Kim, J. H., Sim, J. Y., Kim, C. S.: Video deraining and desnowing using temporal correlation and low-rank matrix completion. IEEE Trans. Image Process., 24 (9), 2658-2670, 2015.

Li, Y., Tan, R. T., Guo, X., Lu, J., Brown, M. S.: Rain streak removal using layer priors. In 2016 IEEE Conference on Computer Vision and Pattern Recognition, IEEE, Las Vegas, NV, 27-30 June, pp. 2736-2744, 2016.

Löffler–Mang, M., Joss, J.: An optical disdrometer for measuring size and velocity of hydrometeors. J. Atmos. Ocean. Technol. 17 (2), 130–139, 2000.

Marshall, J. S., Palmer, W. M.: The distribution of raindrops with size. J. Meteor. 5, 165–166, 1948.

McCabe, M. F., Rodell, M., Alsdorf, D. E., Miralles, D. G., Uijlenhoet, R., Wagner, W., Lucieer, A., Houborg, R., Verhoest, N. E. C., Franz, T. E., Shi, J., Gao, H., Wood, E. F.: The future of earth observation in hydrology. Hydrol. Earth Syst. Sci. 21 (7), 3879-3914, 2017.

Michaelides, S., Levizzani, V., Anagnostou, E., Bauer, P., Kasparis, T., Lane, J. E.: Precipitation: Measurement, remote sensing, climatology and modeling. Atmos. Res. 94 (4), 512.533, 2009.

Nemeth, K., Hahn, J. M.: Enhanced precipitation identifier and new generation of present weather sensor by OTT Messtechnik, In WMO/CIMO Technical Conference, Germany, 2005.

Nottle, A., Harborne, D., Braines, D., Alzantot, M., Quintana-Amate, S., Tomsett, R., Kaplan, L., Srivastava, M. B., Chakraborty, S., Preece, A.: Distributed opportunistic sensing and fusion for traffic congestion detection. In 2017 IEEE SmartWorld, Ubiquitous Intelligence & Computing, Advanced & Trusted Computed, Scalable Computing & Communications, Cloud & Big Data Computing, Internet of People and Smart City Innovation, IEEE, San Francisco, CA, 4-8 August, pp. 1-6, 2017.

Overeem, A., Leijnse, H., Uijlenhoet, R.: Two and a half years of country-wide rainfall maps using radio links from commercial cellular telecommunication networks. Water Resour. Res. 52 (10), 8039-8065, 2016.

Qasim, S., Khan, K. N., Yu, M., Khan, M. S.: Performance evaluation of background subtraction techniques for video frames. In 2021 International Conference on Artificial Intelligence, IEEE, Islamabad, Pakistan, 5-7 April, pp. 102-107, 2021.

https://doi.org/10.5194/amt-2022-196
Preprint. Discussion started: 23 August 2022

Rabiei, E., Haberlandt, U., Sester, M., Fitzner, D.: Rainfall estimation using moving cars as rain gauges–laboratory experiments. Hydrol. Earth Syst. Sci. 17 (11), 4701-4712, 2013.

Rabiei, E., Haberlandt, U., Sester, M., Fitzner, D., Wallner, M.: Areal rainfall estimation using moving cars–computer experiments including hydrological modeling. Hydrol. Earth Syst. Sci. 20 (9), 3907-3922, 2016.

Santhaseelan, V., Asari, V. K.: Utilizing local phase information to remove rain from video. Int. J. Comput. Vis., 112 (1), 71-89, 2015.

Schmidt, J. M., Flatau, P. J., Harasti, P. R., Yates, R. D., Littleton, R., Pritchard, M. S., Fischer, J. M., Fischer, E. J., Kohri, W. J., Vetter, J. R., Richman, S., Baranowski, D. B., Anderson, M. J., Fletcher, E., Lando, D. W.: Radar observations of individual rain drops in the free atmosphere. Proc. Natl. Acad. Sci. 109 (24), 9293-9298, 2012.

Smith, P. L.: Raindrop size distributions: Exponential or gamma—Does the difference matter?. J. Appl. Meteorol. Climatol., 42 (7), 1031-1034, 2003.

Testik, F. Y.: Outcome regimes of binary raindrop collisions. Atmos. Res. 94 (3), 389–399, 2009.

Testik, F. Y., Pei, B.: Wind effects on the shape of raindrop size distribution. J. Hydrometeorol. 18 (5), 1285-1303, 2017.

Tokay, A., Short, D. A.: Evidence from tropical raindrop spectra of the origin of rain from stratiform versus convective clouds. J. Appl. Meteorol. Climatol. 35 (3), 355–371, 1996.

Tripathi, A. K., Mukhopadhyay, S.: Removal of rain from videos: A review. Signal Image Video Process. 8 (8), 1421-1430, 2014.

Trnovszký, T., Sýkora, P., Hudec, R.: Comparison of background subtraction methods on near infra-red spectrum video sequences. Procedia Eng., 192, 887-892, 2017.

Ulbrich, C. W.: Natural variations in the analytical form of the raindrop size distribution. J. Appl. Meteorol. Climatol. 22 (10), 1764–1775, 1983.

Vivekanandan, J., Zhang, G., Brandes, E.: Polarimetric radar estimators based on a constrained gamma drop size distribution model. J. Appl. Meteorol. 43 (2), 217-230, 2004.

Wang, X., Wang, M., Liu, X., Glade, T., Chen, M., Xie, Y., Yuan, Hao., Chen, Y.: Rainfall observation using surveillance audio. Appl. Acoust. 186, 108478, 2022.

Yang, P., Ng, T. L.: Gauging through the crowd: A crowd-sourcing approach to urban rainfall measurement and storm water modeling implications. Water Resour. Res. 53 (11), 9462-9478, 2017.

Yuter, S. E., Houze Jr, R. A.: Measurements of raindrop size distributions over the Pacific warm pool and implications for Z–R relations. J. Appl. Meteorol. 36 (7), 847-867, 1997.

Zen, R., Arsa, D. M. S., Zhang, R., Er, N. A. S., Bressan, S.: Rainfall estimation from traffic cameras. In: Hartmann, S., Küng, J., Chakravarthy, S., Anderst-Kotsis, G., Tjoa, A., Khalil, I. (Eds.) Database and Expert Systems Applications, Springer, Cham, Switzerland, pp. 18-32, 2019.

Zivkovic, Z., Van Der Heijden, F.: Efficient adaptive density estimation per image pixel for the task of background subtraction. Pattern Recognit. Lett. 27 (7), 773-780, 2006.